Numerical Simulation Study of the Effect of Outlet on the Axial Vortex Separator

H. Lou, X. Zhang[†], X. Liu, Y. Wang and R. Liao

Hubei Key Laboratory of Petroleum Drilling and Production Engineering, Wuhan, Hubei, 430100, China
Laboratory of Multiphase Pipe Flow, Gas Lift Innovation Center, China National Petroleum Corp, Yangtze University, Wuhan, Hubei, 430100, China

†*Corresponding Author Email: zhangxingkai@yangtze.edu.cn*

ABSTRACT

This study utilizes numerical simulations and dimensional analysis to investigate the impact of the two-phase outlet on flow field characteristics and separation efficiency of the separator. The study revealed a boundary layer separation at the water outlet, which was subsequently addressed to reduce energy losses in the separator. Dimensional analysis considered the influences of operational, structural, and physical parameters on the separator's performance. With other structural parameters held constant, separation efficiency is directly proportional to the ratio of inlet and oil-outlet diameter. Additionally, the separation efficiency is also associated with Re and the ratio of the inlet to the water-outlet diameter. When the diameter of the water outlet is constant, the axial vortex separator achieves optimal separation when the ratio of inlet and water-outlet diameter is 0.563, with a maximum separation efficiency of 97.00%. The optimal separation efficiency is reached at Re=22,908 under various operational conditions. Separation efficiency increases with water content, peaking at an inlet water content of 0.9 across different structural parameters. Separation efficiency shows an increase followed by a decrease with the rise in inlet flow rate(v_i), achieving the best performance at v_i=3m/s for the different separator structures studied.

1. INTRODUCTION

As oil fields mature and the water content in produced fluids increases year by year, oil-water separation has become increasingly critical in the crude oil extraction process. In the industrial field, cyclone separators are widely used in the energy and chemical industries for their simple structure, compact size, and ease of operation (Zhu et al., 2022). These separators are divided into static and dynamic cyclone separators, with the latter being more efficient. Despite extensive research on cyclone separators (Karagoz et al., 2013), further investigation is needed on how structural and operational parameters affect their separation efficiency and internal flow dynamics (Celis et al., 2022).

Flow performance in cyclone separators has been examined through experimental and computational fluid dynamics (CFD) methods. Chi et al. (2021) designed a liquid-liquid cyclone reactor (LLCR) and applied CFD to study its velocity distribution, pressure, and turbulence fields. Their study found that pressure was primarily concentrated in the cone section and turbulence was most intense near the lateral walls. Additionally, low surface tension and high Weber number were found to positively affect droplet breakage. Zandie et al. (2021) explored the effects of rods with two different designs on the performance of de-oiling hydrocyclones, showing a notable improvement in the overall functionality of the hydrocyclone, enhancement of the flow behavior and separation efficiency compared to the reference model. For an oil particle diameter of 17 μm, separation efficiencies increased by 34.75% and 26.83%, respectively. Zhang et al. (2022) conducted a dimensional analysis and multiphase flow numerical simulation to study the separation process in a cylindrical cyclone with a vortex finder. Their findings indicated that vortices existed in the core of the cylinder, the diameter of the overflow pipe, inlet velocity, and split ratio affected the vortex core structure but had a minimal effect on the core's equivalent diameter. Oil-water separation efficiency increased with the size of the oil droplets; efficiencies exceeded 80% for inlet dispersed droplets larger than 1mm. Kou et al. (2021) presented an innovative axial hydrocyclone separator design that used a guide vane instead of a conventional tangential inlet to reduce inlet turbulence. Their results demonstrated improved flow field symmetry and eliminated the eccentric turbulence typically found in conventional hydrocyclones, thus enhancing oil-water separation.

As a type of dynamic cyclone separator, the axial vortex separator is characterized by its large capacity, high separation efficiency, and strong adaptability (Guizani et al. 2022). The axial vortex separator was developed in the 1990s by the U.S. company EVTN, which designed the Voraxial Separator (VAS) based on axial vortex separation technology principles. From 2004 to 2010, the company conducted on-site experiments with various axial vortex separation equipment in the Gulf of Mexico and achieved positive results. The separators are capable of handling capacities ranging from 450 to 1135 m³/h and can achieve a maximum separation efficiency of 98% (Ji et al., 2015). The Beijing Institute of Petrochemical Technology independently developed the BIPTVAS-I type axial vortex separator for testing (Ji et al., 2012) and engineered the BIPTVAS-II type axial vortex separator prototype based on a comprehensive understanding of the axial vortex separator principle and its basic structure. The field application test was successfully conducted in the LH II-1 oilfield in 2015 (Ji et al., 2017). The results indicated that when the inlet oil content is between 100 and 300 mg/L, the oil removal efficiency can exceed 80%, with the highest efficiency reaching 91.8%, and the oil content in the water outlet can be stabilized at less than 30 mg/L. The optimal operating conditions for this separator were determined to be an inlet flow rate of 3.5 m³/h, a split ratio of 15%, and a vortex generator speed of 1700 rpm. The key factors affecting the separation efficiency of the VAS were analyzed by (Ji et al., 2015). A theoretical model of this new separation technology was established, and a pilot VAS was designed. The results showed that the pilot VAS could achieve a maximum separation efficiency of up to 93%, which occurred when the back-flow ratio was between 2.9% and 11.4%. However, most of the studies on axial vortex separators have been experimental, and the study of their internal flow fields is fewer and incomplete.

The complex internal flow field is crucial to the separation performance of the axial vortex separator (Yu et al., 2021). To better predict the separator's separation efficiency and design a more efficient separator, it is important to understand the internal flow field distribution characteristics and the effect of various structural parameters on the internal flow field (Gorman et al., 2016). In this paper, Ansys fluent software is utilized to study the internal flow field distribution characteristics of the axial vortex separator and the influence of the separator's two-phase outlet structure on the internal flow field and separation performance. This research aims to further optimize the separation performance of the axial vortex separator and provide a reference for addressing oil-water separation challenges.

2. STRUCTURE AND WORKING PRINCIPLE

Figure 1 depicts a schematic diagram of the axial vortex separator's structure, which is comprised of three components: the mixed fluid inlet, the rotating barrel, and the stationary barrel. The rotating barrel is equipped with a set of spiral blades. The stationary barrel consists of the conical barrel, oil outlet, and water outlet. The spiral blade is positioned at the near inlet end of the rotating barrel and is welded to its inner wall. Its length is half that of the rotating barrel, and the blade's height is less than the rotating barrel's radius. The oil outlet is situated on the separator's central axis and is installed at the stationary barrel's end. The water outlet is placed at the end of the separator, with its opening directed downward, in line with gravity.

During operation, the rotating barrel begins to rotate via an external drive. The oil-water mixture enters the rotating barrel from the axial vortex separator's inlet with a certain axial velocity and undergoes high tangential velocity cyclonic motion, driven by the high-speed rotating spiral blades. Due to centrifugal force, the less dense oil phase gathers at the axis, forming an oil core within the separator, while the denser water phase moves toward the separator's wall. The oil core exits through the oil outlet, propelled by axial velocity and the pressure differential between the separator and the external environment, while the water phase is expelled through the water outlet along the sidewall, thus achieving oil-water separation.

3. NUMERICAL SIMULATION

3.1 Numerical Model

3.1.1 Basic Assumptions

We assume that the turbulent oil-water flow is the flow of two immiscible fluids (Kou et al., 2021), with both fluids being incompressible. The temperature within the flow field is assumed to be the same as the external environment, and there is no energy transfer to or from the outside. The disruption of oil droplets and the interactive forces between them during the separation process are disregarded, and the flow of the continuous phase is not influenced by the dispersed phase.

3.1.2 Multiphase Flow Model

Two flow models are typically employed for multiphase flow simulations: the Eulerian-Lagrange and Eulerian-Eulerian models. The Eulerian-Lagrange model is applied for calculating two-phase flows where one phase is dispersed and the volume fraction of the dispersed phase is less than 10%. The Eulerian-Eulerian model encompasses Eulerian, Mixture, and Volume of
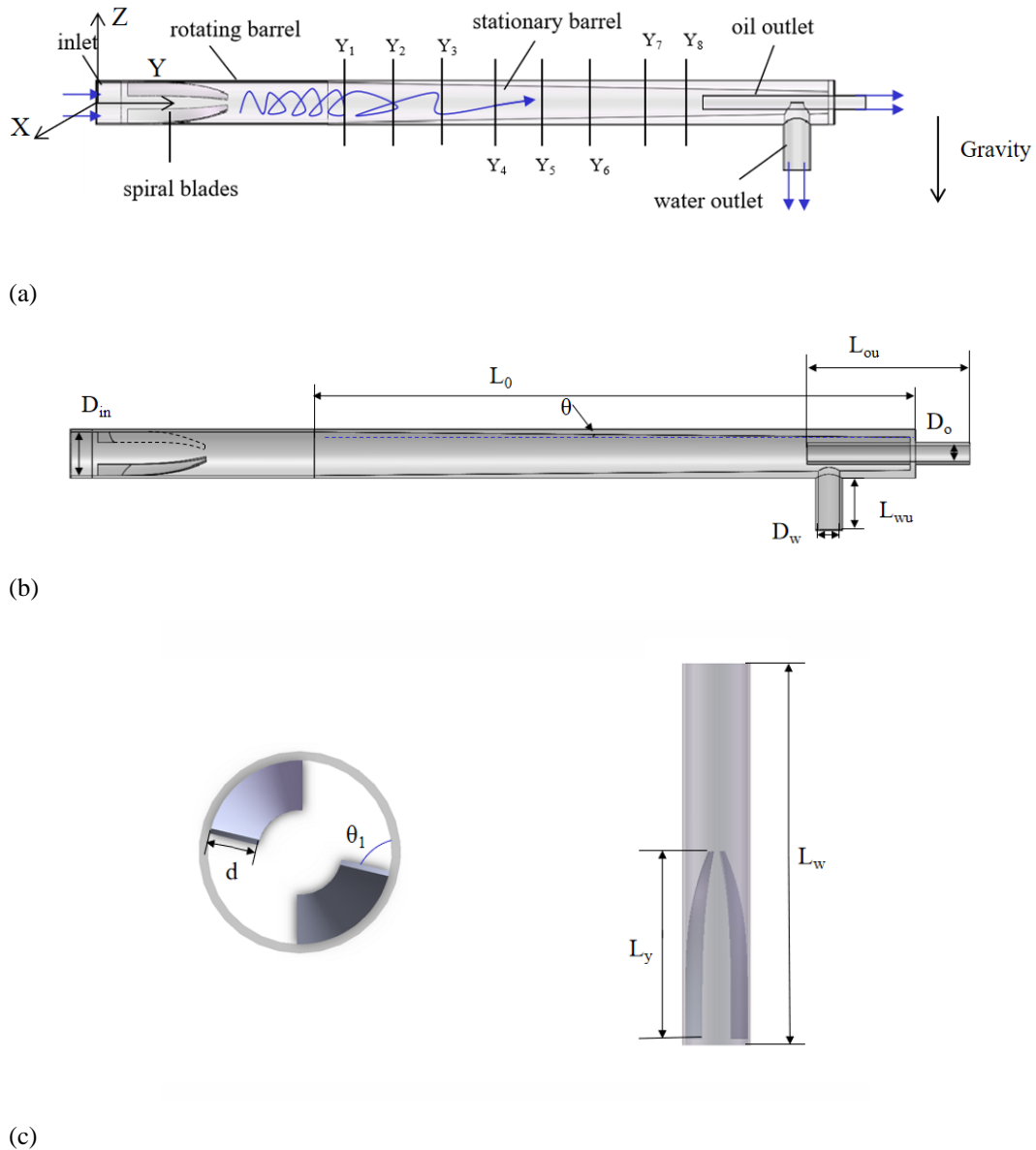
(a)

(b)

(c)

Fig. 1 Schematic diagram of the structure of the axial vortex separator

Table 1 Main structural parameters of axial vortex separator

Parameters	L_w	L_y	n	θ	θ_1	L_{ou}
Numerical Value	400mm	200mm	2	1.04°	64°	300mm
Parameters	D_w	D_o	d	D_{in}	L_0	L_{wu}
Numerical Value	40mm	30mm	13mm	80mm	1100mm	100mm

Fluid (VOF) models, which are interface capture models appropriate for characterizing bicontinuous two-phase flows. In this study, the VOF model (Chi et al., 2021) is utilized, suitable for transient multiphase flow, and the outcomes produced by this model provide a distinct separation interface between the oil and water phases, allowing for more straightforward observation of the oil-water separation process. At the mixture inlet, the calculation accuracy of the VOF model is relatively low, but as long as the grid resolution is sufficiently high, the calculation accuracy will improve without affecting the downstream results. In the downstream separation, where oil and water are fully separated and only one fluid exists within the cells, the VOF model can achieve precise computational results. For the VOF model, when there are more neighboring cells with the mixture, then the interface cannot be identified. However, if the mesh accuracy is high enough, there will only be one type of fluid in the cells, and the VOF model can accurately identify the interface between the two phases.

The VOF model is predicated on the control equation for each phase's volume fraction and delineates the interaction between phases by monitoring the interface location. By solving each phase's volume fraction conservation equation to depict the multiphase flow, the volume fraction equation for each phase is:

$$\frac{\partial \alpha_i}{\partial t} + \nabla \cdot (\alpha_i \mathbf{V}) = 0 \qquad (1)$$

where i denotes different phases, α_i is the volume fraction of phase i, and $\mathbf{V}$ represents the velocity vector of the phases. This equation characterizes the temporal and spatial changes in each phase's volume fraction. Through volume fraction computation, it is possible to ascertain the interaction and interface location between phases.

The continuity equation is (Abrahamson, 2020):

$$\frac{\partial (\alpha_i \rho_i)}{\partial t} + \nabla \cdot (\alpha_i \rho_i \mathbf{V}) = 0 \qquad (2)$$

where ρ_i is the density of the i phase. This equation indicates that within the unit of time, the quality of each grid unit is conserved.

The momentum equation is as follows (Abrahamson, 2020; Boruah et al., 2021):

$$\frac{\partial (\alpha_i \rho_i \mathbf{V})}{\partial t} + \nabla \cdot (\alpha_i \rho_i \mathbf{V} \times \mathbf{V}) = -\nabla p_i + \nabla \cdot \boldsymbol{\tau}_i + \mathbf{f}_{si} + \mathbf{f}_{vi} \qquad (3)$$

Where p_i represents the pressure in phase i, $\boldsymbol{\tau}_i$ denotes the stress tensor in phase i, and $\mathbf{f}_{si}$ and $\mathbf{f}_{vi}$ express the surface tension and volume force, respectively. This equation governs the motion of each phase, taking into account factors such as inertia, pressure, and viscosity.

3.1.3 Turbulence Models

This study adopts the RNG k-ε model, which modifies the coefficient values and includes additional dissipative terms compared to the standard k-ε model. The transport equations are as follows (Abrahamson, 2020; Zhang et al., 2022):

$$\frac{\partial}{\partial t}(\rho k) + \frac{\partial}{\partial x_i}(\rho k u_i) = \frac{\partial}{\partial x_i}\left(\alpha_k \mu_{\text{eff}} \frac{\partial k}{\partial x_i}\right) + G_k - \rho \varepsilon + S_k \qquad (4)$$

The RNG k-ε model turbulent dissipation rate transportation equation is：

$$\frac{\partial}{\partial t}(\rho \varepsilon) + \frac{\partial}{\partial x_i}(\rho u_i \varepsilon) = \frac{\partial}{\partial x_i}\left(\alpha_\varepsilon \mu_{\text{eff}} \frac{\partial \varepsilon}{\partial x_i}\right) + \frac{\varepsilon}{k}(C_{\varepsilon 1} G_k - C_{\varepsilon 2} \rho \varepsilon) - R_\varepsilon + S_\varepsilon \qquad (5)$$

where G_k represents the turbulent generation item caused by the average speed gradient; α_k expresses the countdown of the Prandtl number of k; α_ε denotes the countdown of the Prandtl number of ε; μ_{eff} is the effective turbulent viscosity, Pa·s; S_k and S_ε are the source items.

3.2 Parameter Settings and Boundary Conditions

In this study, the transient flow field within the axial vortex separator is numerically simulated using Fluent software. A full-size 3D model is selected, utilizing a double-precision implicit solver and a pressure-based solver. Given that the primary motion in the separator's flow field is vortex motion, an algorithm with higher accuracy for calculating vortex motion is chosen; specifically, the SIMPLE algorithm, based on the finite volume method, is used for solving, while other equations employ the higher-order Quick algorithms (Gong et al., 2023).

The density of the oil phase is set at 850kg/m³, and that of the water phase at 998.2kg/m³. The power viscosity of the oil phase is 60mPa·S, and that of the water phase is 1.003mPa·S. The water phase is considered the first phase, and the oil phase is the second phase. The fluid in the rotating barrel section of the machine is configured using the slip grid method, assuming a perfectly symmetrical inlet and no slip at the walls. The corresponding wall surface is designated as a rotating wall, with its speed relative to the adjacent fluid domain remaining stationary. The junction between the stationary conical barrel and the rotating barrel is defined as the interface, and the barrel wall surface is set as a stationary no-slip wall. The inlet boundary condition is specified as a velocity inlet with an initial velocity between 2~4m/s, and the inlet water volume fraction is between 0.7-0.9. The outlet boundary condition is defined as an outflow. A split ratio of 1 is chosen. The rotating barrel operates at a speed of 2000r/min, with the rotation axis along the Y-axis.

3.3 GRID DIVISION AND GRID INDEPENDENCE

3.3.1 Grid Division

The numerical simulation relies on a three-dimensional model. Initially, geometric modeling is completed in SolidWorks, followed by importation into ANSYS SpaceClaim for geometric pre-processing, which includes segmenting the fluid domain and naming the faces and bodies. The widespread adoption of Fluent Meshing's polyhedral meshing technique not only reduces meshing time but also significantly enhances mesh quality. The grid orthogonality quality exceeds 0.2, and the skewness is kept below 0.5 (Zandie et al., 2021). A boundary layer is added to the separator's wall surface, and grid refinement is conducted in complex regions such as the spiral blades to ensure the accuracy of the computational results. The grid model is illustrated in Fig. 2.

3.3.2 Y-plus

Y^+ is a dimensionless distance representing the ratio of the distance from the wall to a point to the characteristic length scale. It is commonly used to determine the mesh's coarseness or fineness for a given flow pattern. Different turbulence models and wall functions impose various requirements on the y^+ value at the wall. It is important to note that higher wall flow velocities necessitate higher y^+ values. Consequently, the mesh size near the wall must be reduced. Given that the standard wall function and the k-ε model are used, the y^+ value of the mesh's first layer near the wall should ideally fall between 30 and 300 (Zandie et al., 2021). The y^+ values for the grids used in this study all meet the specified range.

3.3.3 Grid Independence

The VOF model places high demands on grid precision (Baker, 2023). To eliminate the impact of mesh count on the accuracy of the results and to minimize computational load on the computer, a mesh-
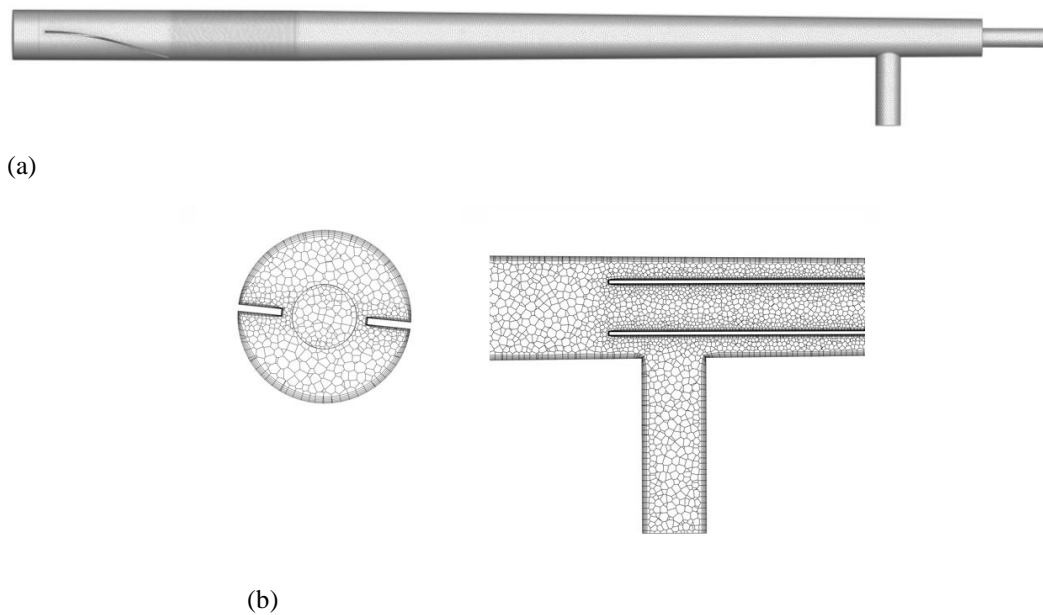
(a)

(b)

Fig. 2 Axial vortex separator grid model

Table 2 Grid independence verification

Grid Number	Separation Efficiency/%	Water outlet Flow Velocity /m/s	Oil outlet Flow Velocity /m/s
725,674	79.88	7.9900	8.8846
913,258	86.52	7.7241	8.7498
1,025,474	95.79	7.1241	8.6498
1,193,662	95.86	7.1232	8.6512
1,385,766	95.75	7.1248	8.6488

independence test is essential (Dyakowski & Williams, 1993; Clausse & López De Bertodano, 2021). The axial vortex separator is divided into five grid models with grid counts of 725,674; 913,258; 1,025,474; 1,193,662; and 1,385,766. Table 2 presents the separation efficiency and two-phase outlet flow rates for each grid model under identical structural and operational conditions. The oil-water separation efficiency of an axial vortex separator is defined by the ratio of the oil phase flow rate at the oil outlet to the inlet oil phase flow rate, and the separation efficiency is calculated as follows (Ji et al., 2015):

$$\eta = \frac{Q_{oo}}{Q_{io}} \qquad (6)$$

where η is the separation efficiency; Q_{oo} is the oil phase flow rate in the oil outlet, kg/s; Q_{io} is the inlet oil phase flow rate, kg/s.

Figure 3 presents the tangential velocity distribution at the Y_5 section, for each grid model under identical structural and operational conditions. It is evident from the Table 2 and Fig 3 that the variation in results becomes negligible when the grid count exceeds 1,000,000. Calculations with fewer than 1 million grids show significant variability and lack stability in separation efficiencies and velocities. For a balance of computational efficiency and accuracy, this study selects a grid model with approximately 1 million cells for simulation calculations.
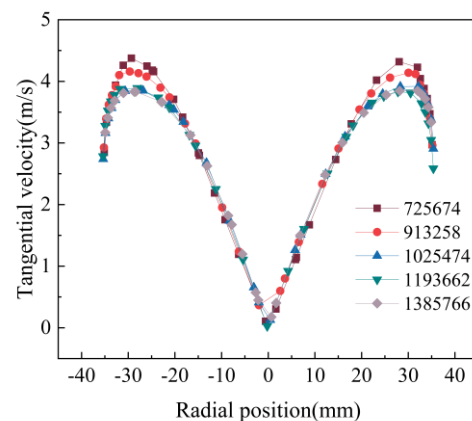

Fig. 3 Tangential velocity distribution of different grid models at the Y_5 section

4. VALIDATION OF RESULTS

To assess the accuracy of the findings of this study, the research works of Ji et al. (2015) and Ji (2015) were referenced. A numerical simulation of an axial vortex separator with the same structural parameters as in Ji (2015) was performed under identical conditions. The inlet flow varied from 3m³/h to 6m³/h，and the rotation speed varied from 1500rpm to 2400rpm. To keep the inlet oil volume fraction is 0.1. The structural parameters

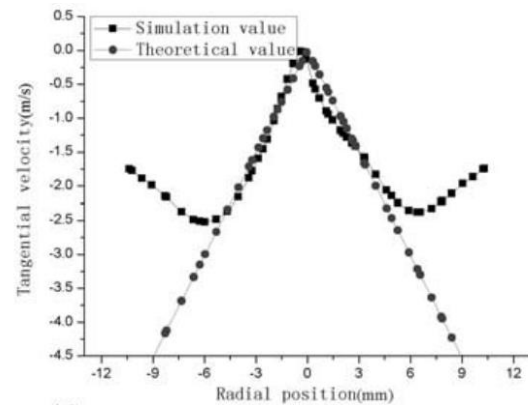**Table 3 Comparison of Numerical and Experimental Data**

Inlet Flow/m³/h	Rotation Speed/rpm	Separation Efficiency/%		Relative Error/%
		Experimental	Numerical	
3	1500	76.0	78.8	3.68
4	1800	84.0	87.2	3.81
5	2100	87.0	88.5	1.72
6	2400	83.0	86.9	4.70

Table 4 Main structural parameters of the validation model

Parameters	L_w	L_y	n	θ	θ_1	L_{ou}
Numerical Value	320mm	170mm	2	1.43°	72°	300mm
Parameters	D_w	D_o	d	D_{in}	L_0	L_{wu}
Numerical Value	40mm	30mm	21.5mm	60mm	980mm	100mm
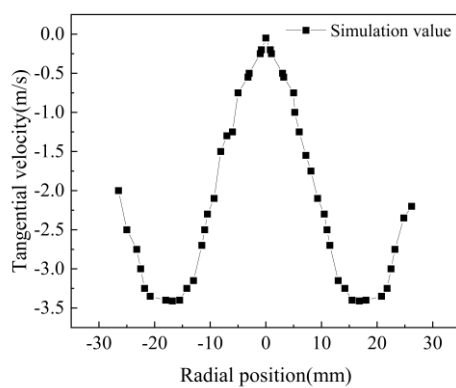
(a)   (b)

Fig. 4 Comparison of numerical(a) and references(b) tangential velocity distribution

are as shown in Table 4.

The simulation outcomes were compared with the experimental results from Ji (2015), as depicted in Table 3. Although the simulated data are marginally higher than the experimental data, the discrepancy is within an acceptable range of 5%. The simulation results were compared with those of Ji et al. (2015), as shown in Fig. 4. Figure 4(a) represents the simulation results of this study, and Fig. 4(b) denotes the simulation results of Ji et al. (2015). It can be observed from the figure that their tangential velocity distribution follows the same pattern.

The agreement between the experimental and simulated results confirms the capability of the numerical model used in this study to predict the separation performance of the axial vortex separator accurately.

5. FLOW FIELD ANALYSIS

The diameters of the two-phase outlets in the axial vortex separator, D_w and D_o, significantly affect the flow field distribution within the separator. Adjusting these diameters can directly alter the pressure differential across the separator and influence the flow field distribution, thereby affecting the separator's performance (Liu et al., 2012; Zhang et al., 2022). The simulation examined the effects of varying structural

parameters of the two-phase outlet under operating conditions with an oil-water mixture inlet flow rate of 3 m/s, a rotating barrel speed of 2000 rpm, and the inlet water content of 90%.

5.1 Concentration Field

The axial vortex separator has a water outlet diameter of 40 mm and an oil outlet diameter of 30 mm. The distribution of the oil phase across the barrel's radial section at distances from the separator inlet of $Y_1 = 510mm$, $Y_2 = 610mm$, $Y_3 = 710mm$, $Y_4 = 810mm$, $Y_5 = 910mm$, $Y_6 = 1010mm$, $Y_7 = 1110mm$ and $Y_8 = 1210mm$ is illustrated in Fig 5 and 6. These figures show that from the wall to the center axis, the oil phase's volume fraction gradually increases, with the densest distribution near the core of the separator. The volume fraction of the oil phase at the center of the shaft is higher the further it is from the inlet end, indicating that the longer the oil droplets are subjected to centrifugal forces, the more concentrated they become. Nearer the outlet section, some oil droplets adhere to the wall but eventually detach under centrifugal forces to coalesce at the barrel's central shaft, forming an oil core. The closer to the outlet, the smaller the oil core's diameter and the higher the oil phase's volume fraction, which facilitates the entry of the oil into the collection tube and thereby enhances oil-water separation (Ji et al., 2015).
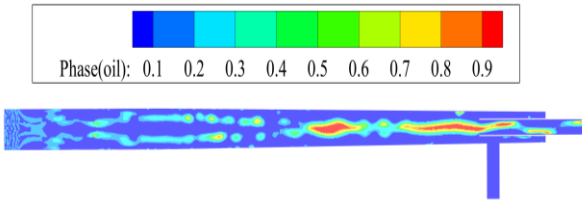
Fig. 5 Cloud diagram of oil phase distribution in the separator（D_w=40mm, D_o=30mm）

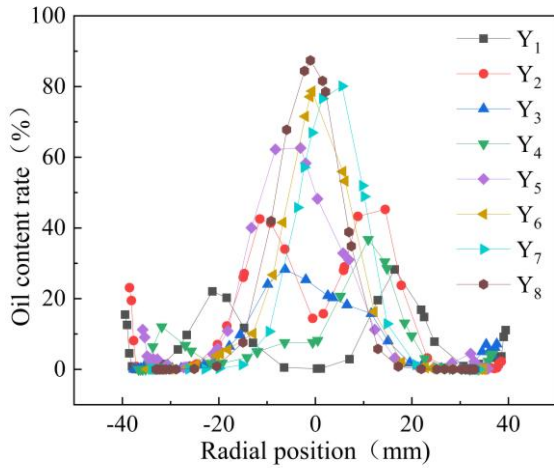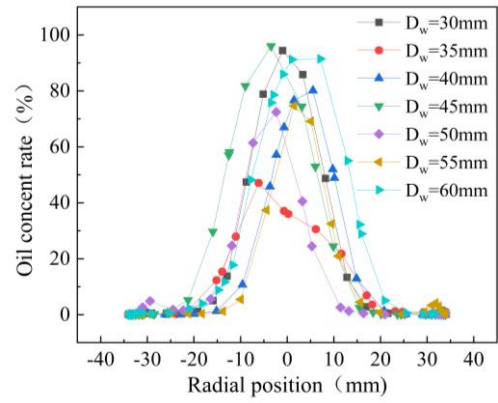**Fig. 6 Oil phase distribution at different cross sections（D_w=40mm, D_o=30mm）**

(a)

(b)

Fig. 7 Distribution of oil phase with different outlet diameters at the Y_7 section
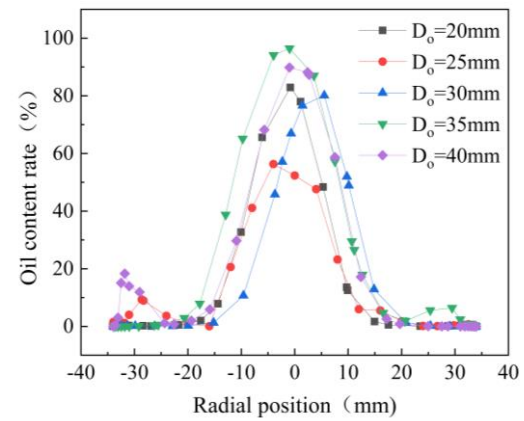
The distribution of the oil phase on the Y_7 cross-section for separators with varying two-phase outlet diameters is depicted in Fig. 7. The figures indicate that altering the outlet diameter does not significantly impact the distribution of the oil phase within the separator. The oil phase remains concentrated around the barrel's shaft area, and the diameter of the two-phase outlets has a marginal effect on the diameter of the oily core at the cross-section. Figure 7(a) shows that the maximum oil phase concentration is 96.00% when the diameter of the water outlet is 45 mm, whereas the maximum oil phase concentration at the cross-section drops to 47.07% when the diameter is reduced to 35 mm, a difference of nearly 50%. According to Fig. 7(b), the maximum oil phase concentration reaches 96.46% with an oil outlet diameter of 35 mm, in contrast to only 55.96% when the diameter is 25 mm, demonstrating a difference of 40.50%. Consequently, neither a larger nor a smaller diameter for the oil or water outlet is optimal for achieving the most effective convergence of oil droplets. An appropriate intermediate diameter seems to facilitate better convergence of oil droplets.

5.2 Pressure Field

The pressure distribution within the axial vortex separator significantly influences its separation performance (Young et al., 1994). The radial pressure gradient is a crucial factor in the aggregation of oil droplets. Figures 8 and 9 illustrate the pressure distribution in the axial vortex separator with a water outlet diameter of 40 mm and an oil outlet diameter of 30 mm.
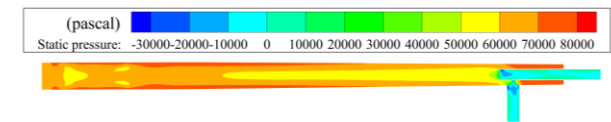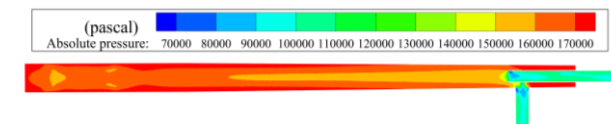

(a)

(b)

Fig. 8 Pressure distribution cloud in the separator

As observed in Fig. 9, within the radial direction of the axial vortex separator, the pressure decreases closer to the axis, with the highest pressure near the wall of the tube. The pressure differential from the wall to the axis at each cross-section is approximately 15 kPa. This pattern arises because the fluid, when accelerated by the rotating mechanism and pushed by the spiral blades, experiences an increase in flow and pressure along the barrel wall surface while a low-pressure and low-speed zone is formed near the axis. In the axial direction, the pressure
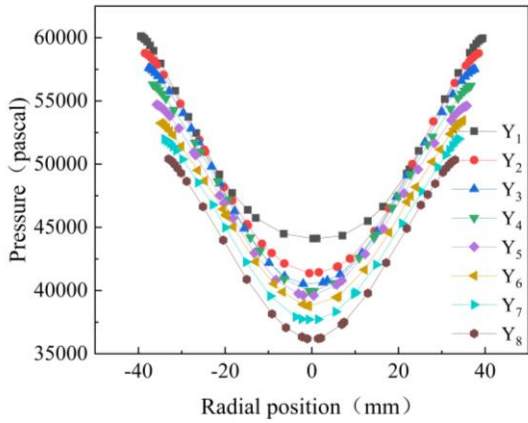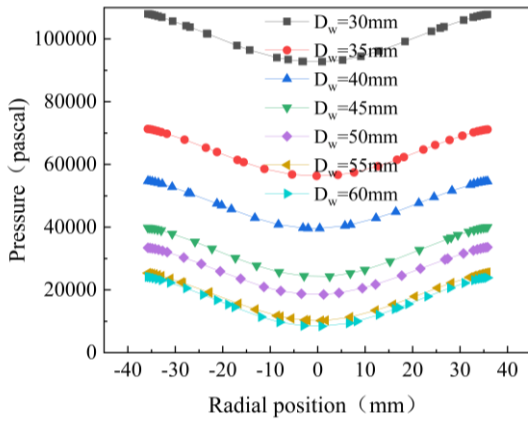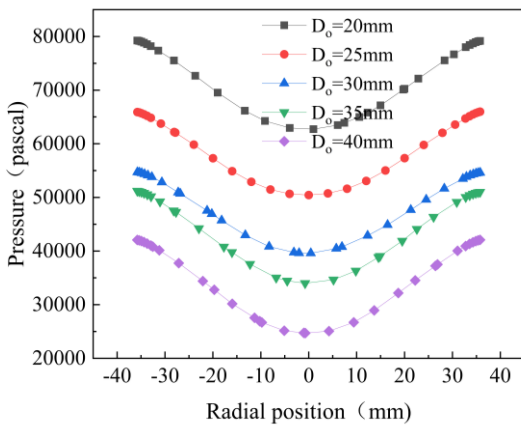
Fig. 9 Pressure distribution diagram of different sections（D_w=40mm, D_o=30mm）

(a)

(b)

Fig. 10 Relative pressure distribution of different outlet diameters at the Y_5 section

(a)

(b)

Fig. 11 Effect of two-phase outlet diameter on the radial pressure difference

higher pressure within the barrel, suggesting that the outlet diameter substantially affects the pressure inside the separator. Figure 10 (a) shows that when the water outlet diameter is small, its effect on the separator's pressure is more pronounced. However, as the diameter of the water outlet increases, the impact of its size on the pressure becomes less significant. Consequently, it may be inferred that beyond a certain point, enlarging the water outlet diameter has a negligible effect on the internal pressure of the separator. From Fig. 10(b), it is observed that within the examined range, as the diameter of the water outlets increases, the pressure decrease in the separator does not follow a specific trend.

Figure 11 illustrates the impact of various two-phase outlet diameters at different cross-sections on the radial pressure difference within the separator. Figure 11(a) indicates that across the range of water outlet diameters, the radial pressure difference between the wall surface and the axis across different sections exhibits minor fluctuations, and no clear pattern of change is apparent. While the diameter of the aqueous phase outlet can influence the pressure field size inside the separator to a certain extent, it has a limited effect on the radial pressure difference. As shown in Fig. 11(b), with an increase in the oil outlet diameter, the internal radial pressure difference within the separator displays a trend

decreases closer to the outlet end since the two-phase outlets are exposed to atmospheric pressure, and Fig. 8 presents a consistent distribution law.

Figure 10 displays the pressure distribution on the Y_5 cross-section for separators with diverse two-phase outlet diameters. It is apparent that, at the same cross-sectional position, a larger two-phase outlet diameter results in
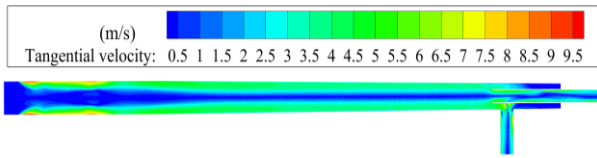
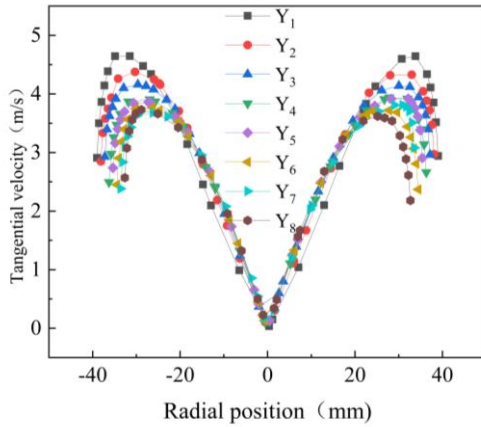**Fig. 12 Cloud diagram of tangential velocity distribution（D_w=40mm, D_o=30mm）**

Fig. 13 Tangential velocity distribution of different sections (D_w=40mm, D_o=30mm)

of initially decreasing and then increasing. In the oil outlet diameter range of 20 mm to 35 mm, the rate of change is significant. Once the diameter of the oil outlet exceeds 35 mm, the radial pressure difference tends to stabilize.

5.3 Speed Field

5.3.1 Tangential Velocity

The tangential velocity imparted by the high-speed rotating spiral blades plays a crucial role in establishing the vortex flow of fluid within the separator and is the primary source of centrifugal force that influences the convergence of oil droplets towards the axis. The tangential velocity is critical for the separation performance of the axial vortex separator. The fundamental fluid motion within the axial vortex separator is a combined Rankine vortex (Aghaee et al, 2017). For two ideal states of fluid performing a vortex motion, the distribution of tangential velocity can be represented by two types: the forced vortex and the free vortex. The tangential velocity distribution of the fluid in the separator adheres to the Rankine combined vortex tangential velocity calculation equation (Al-Kayiem et al., 2020):

$$u_\theta r^n = C \tag{7}$$

where u_θ is the tangential velocity of the liquid in the separator, m/s; r is the radius of any position, m; C is a constant, related to the separator operation and structural parameters; A is an exponent, and associated with many parameters.

Figures 12 and 13 depict the tangential velocity distribution in the axial vortex separator with water and

oil outlet diameters of 40 mm and 30 mm, respectively. It is evident that the tangential velocity distribution at each cross-section in the separator conforms to the Rankine combined vortex tangential velocity distribution formula. Within the forced vortex, the tangential velocity of the fluid gradually increases from the axis outward and reaches a peak at the boundary of the vortex core. In the free vortex, the tangential velocity of the fluid gradually decreases from the vortex core boundary towards the separator wall. Along the axial direction, both the radius of the vortex core and the tangential velocity display a decreasing trend as they approach the outlet end. The simulation results align with theoretical analysis.

Figure 14 presents the tangential velocity distribution at the Y_5 cross-section in the axial vortex separator with different two-phase outlet diameters. It is observed that the tangential velocity distributions at the same cross-section for separators with varying two-phase outlet diameters almost completely overlap. The two-phase outlet diameters do not significantly affect the distribution of tangential velocity within the separator. As previously discussed, the two-phase outlet diameter is directly connected to the pressure magnitude within the separator; thus, the tangential velocity distribution is also independent of the pressure field size within the separator.
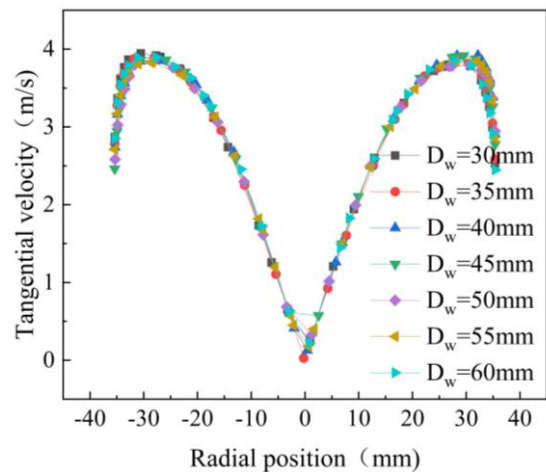
(a)
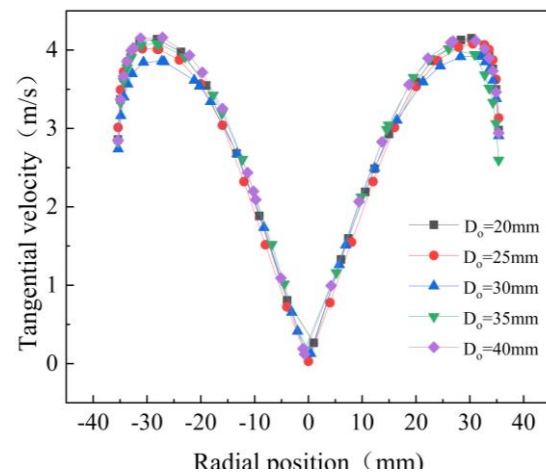
(b)

Fig. 14 Tangential velocity distribution of different outlet diameters at the Y_5 section
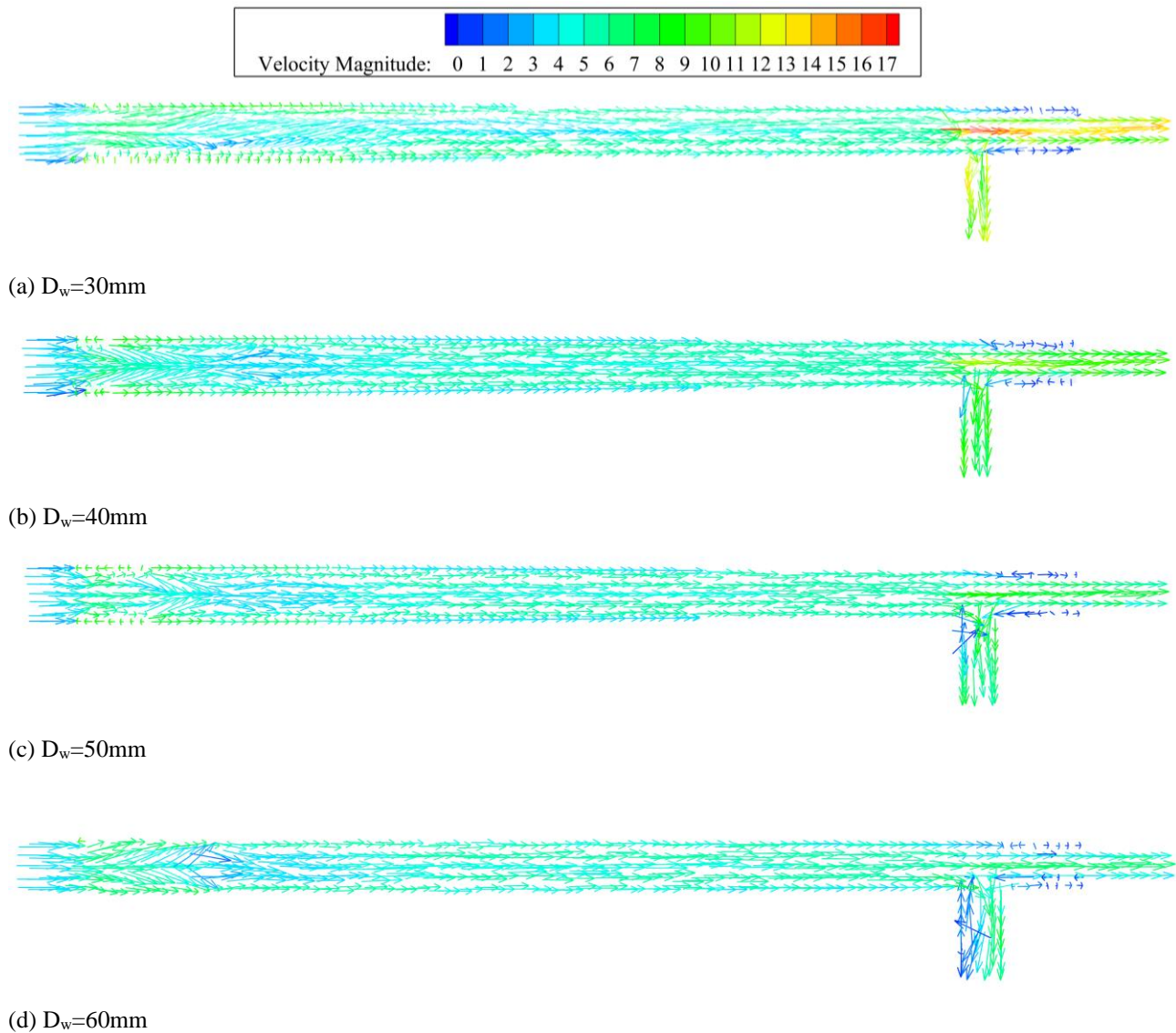
(a) D_w=30mm

(b) D_w=40mm

(c) D_w=50mm

(d) D_w=60mm

Fig. 15 Velocity vector diagram of the axial section with different water outlet diameters

5.3.2 Velocity Vector

Figure 15 illustrates the velocity vectors on the axial section of the separator with varying water outlet diameters. The velocity size within the separator barrel is consistent, and the size and distribution of the combined velocity within the barrel remain the same for different water outlet diameters. It is evident that a change in the water outlet diameter does not impact the velocity distribution within the separator barrel. As the fluid moves towards the oil and water outlets in the barrel, there is a notable and sudden increase in flow rate. Furthermore, as the water outlet diameter decreases, the flow rate at both the oil and water outlets increases. As discussed in the previous section, a smaller water outlet diameter results in higher pressure inside the separator. With the two-phase outlet pressure remaining constant, the pressure difference at the outlets becomes larger, and consequently, the rate at which fluid flows out of the separator increases. These findings are in line with theoretical analysis.

Figure 16 presents the local velocity vector diagram at the oil and water outlets of the separator when the water outlet diameter is 30 mm, 40 mm, 50 mm, and 60 mm. It can be observed that as the water outlet diameter increases to 40 mm, a reflux zone near the left side of the barrel end wall expands. When the water outlet diameter reaches 60 mm, the reflux area within the water outlet nearly occupies half of the entire outlet area. The vector diagram indicates that the vector arrows in the reflux region are sparse, signifying that the liquid is flowing back at a very low flow rate in this region. The presence of this low-speed reflux zone reduces the effective outflow area of the liquid at the aqueous phase outlet, resulting in the actual outflow being less than the theoretical outflow.

5.4 Low-speed Reflux Zone Problem Analysis and Solution

The low-velocity reflux area is essentially a manifestation of boundary layer separation. As the liquid flows through the aqueous phase outlet, with a sudden change in flow direction and tube diameter, boundary layer separation occurs due to viscosity and adverse pressure gradient. This phenomenon can increase flow resistance and cause significant flow losses (Versteeg & Malalasekera, 2007). The pressure drop and downstream dynamic pressure are commonly used in engineering to
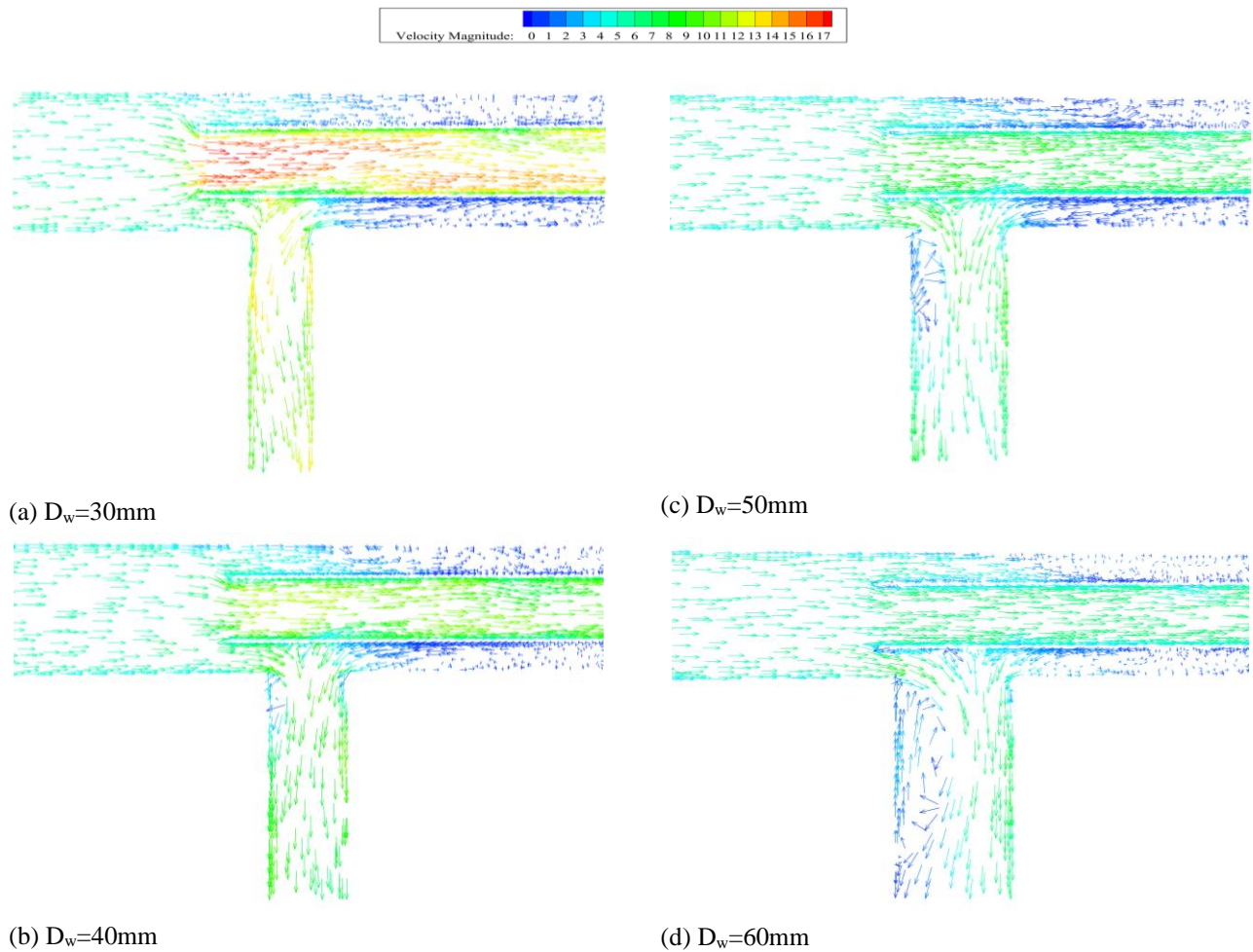
(a) D_w=30mm

(c) D_w=50mm

(b) D_w=40mm

(d) D_w=60mm

Fig. 16 Local velocity vector diagram of the axial section with different water outlet diameters

Table 5 Table of loss coefficients for different water outlets

Outlet Type	40mm		50mm		60mm	
	Right angles	Rounded angles	Right angles	Rounded angles	Right angles	Rounded angles
Outlet velocity （m/s）	6.688	8.363	5.656	6.808	4.613	5.308
Outlet Pressure Drop （pa）	13494.008	1068.304	5573.921	2808.891	1454.965	874.802
Loss Coefficient	0.605	0.031	0.349	0.121	0.137	0.062

define the loss coefficient.

$$K_L = \frac{\Delta p_t}{\rho V^2 / 2} \tag{8}$$

The boundary layer separation can be effectively mitigated by softening the abruptness of the tube diameter reduction. In this study, the low-velocity reflux zone at the water-phase outlet is addressed by transitioning to a rounded constriction. As depicted in Fig. 17, a more uniform velocity distribution is observed at the rounded contraction water outlet, and the low-speed reflux zone is significantly diminished or even eliminated.

The loss coefficients calculated for different water outlets are presented in Table 5. It is apparent that after modifying the water outlet to a rounded constriction, the

flow rate at the outlet increases, the pressure drop decreases, and the loss coefficient is significantly reduced, which in turn diminishes the energy loss in the separator.

Figure 18 compares the separation efficiency with different types of aqueous phase outlet. The results indicate that the separation efficiency improves after transitioning to a rounded constriction water outlet, though the improvement is marginal.

In summary, changing the water outlet to a rounded constriction can significantly reduce the adverse effects of boundary layer separation. Although the increase in separation efficiency of the axial vortex separator is modest, it can significantly decrease the loss coefficient and reduce energy loss, enabling the liquid exiting the separator to maintain a high flow rate.
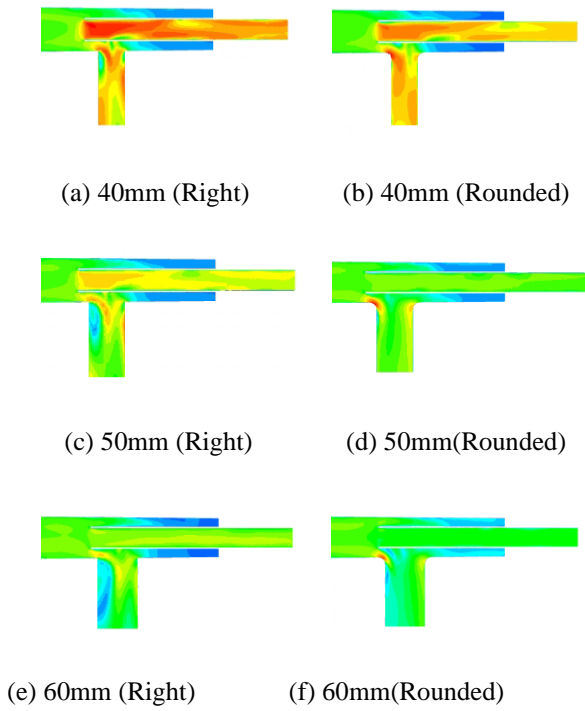
(a) 40mm (Right)   (b) 40mm (Rounded)

(c) 50mm (Right)   (d) 50mm(Rounded)

(e) 60mm (Right)   (f) 60mm(Rounded)

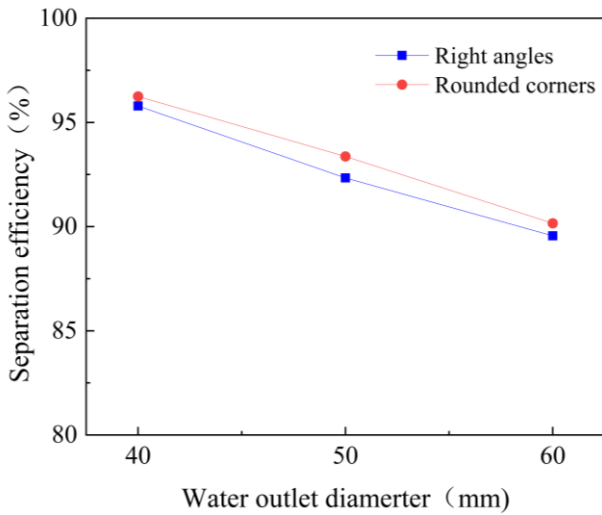**Fig. 17 Local velocity clouds of two water outlets**

Fig. 18 Separation efficiency of different water outlet types

6. SEPARATION PERFORMANCE ANALYSIS

6.1 Influencing Factors and Quantitative Analysis

The separation performance of the axial vortex separator is affected by various factors, which include structural parameters, operational parameters, and physical parameters. Structural parameters primarily refer to the separator's geometric dimensions, such as the length of the vortex generator (L_w), the length of the spiral blade (L_y), the number of blades (n), the inlet diameter (D_{in}), the length of the static barrel (L_0), the cone angle of the barrel (θ), the diameter of the water outlet (D_w), and the diameter of the oil outlet (D_o).

Operational parameters cover the inlet flow rate (v_i) and inlet water content (ε). Physical properties consider the viscosity (μ_w) and density (ρ) of water, and the viscosity (μ_o) and density (ρ_o) of oil. Consequently, the separation efficiency (η) of the axial vortex separator can be expressed as a function of these variables:

$$\eta = f(L_w, L_y, n, D_{in}, L_0, \theta, D_w, D_o, v_i, \varepsilon, \mu_w, \rho_w, \mu_o, \rho_o, ...)$$

(9)

This paper concentrates on the impact of the two-phase outlet on the axial vortex separator. By keeping the other structural dimensions constant and under specified inlet conditions, the following expressions are derived from dimensional analysis (Liu et al., 2012; Zhang et al., 2022):

$$\eta = f\left(Re, \frac{D_w}{D_{in}}, \frac{D_o}{D_{in}}\right)$$

(10)

$$Re = \frac{\rho_m D_{in} v_i}{\mu_m}$$

(11)

where ρ_m is the density of the mixture; μ_m is the mixture viscosity. The principle of controlling variables is generally used in the study, which can be simplified into the following two expressions:

$$\eta = f\left(Re, \frac{D_w}{D_{in}}\right)$$

(12)

$$\eta = f\left(Re, \frac{D_o}{D_{in}}\right)$$

(13)

The density and viscosity of oil-water mixtures are calculated as follows:

$$\rho_m = \varepsilon \rho_w + (1 - \varepsilon)\rho_o$$

(14)

$$\ln \mu_m = x_w \ln \mu_w + x_o \ln \mu_o$$

(15)

where x_w is the molar fraction of water; x_o is the molar fraction of oil; ε is the inlet water content.

Thus, it is evident that the separation efficiency of the axial vortex separator is influenced by the Reynolds number and the ratio of outlet to inlet diameters, with other structural parameters held constant.

6.2 Influence of The Ratio of Inlet and Outlet Diameter on the Separation Performance

Numerical simulations of the axial vortex separator structure with varying inlet and outlet diameter ratios at different Reynolds numbers are conducted at a rotational speed of 2000 rpm for the barrel. The expression for the Reynolds number indicates that its magnitude is primarily determined by the mixture's inlet flow rate and water content. Therefore, this section investigates the effect of different Reynolds numbers and inlet diameter ratios on the separator's separation performance from two perspectives: inlet flow rate and water content.

Separation performance is the primary criterion for evaluating a separator's effectiveness, and separation efficiency is commonly used to characterize a separator's performance in the field of multiphase separation.
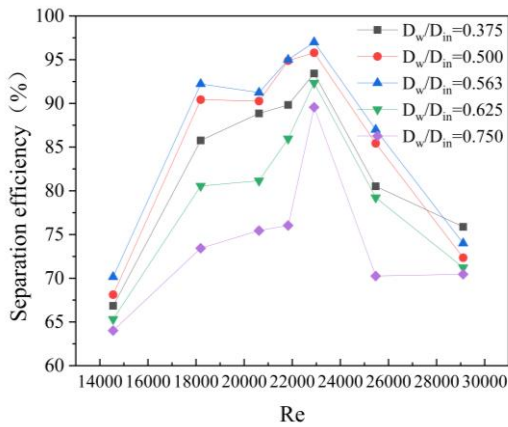
6.2.1 Effect of the ratio of water outlet to inlet diameter on the separation performance

As indicated by equation (12), under the condition that other structural parameters are constant, the separation efficiency of the separator is a function of both the Reynolds number and the ratio of the water outlet to inlet diameter. The relationship curves between Re and D_w/D_{in} on the separation performance, obtained through numerical simulation, are displayed in Fig. 19.

From Fig. 19(a), it can be observed that the separation efficiency initially increases with the ratio of the aqueous phase outlet to the inlet diameter and then decreases, with the optimal separation effect occurring when D_w/D_{in} equals 0.563. When D_w/D_{in} is less than
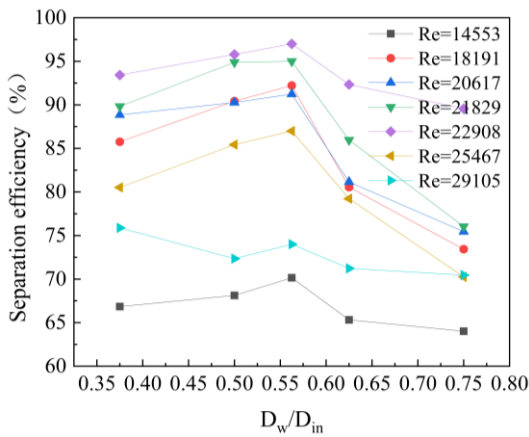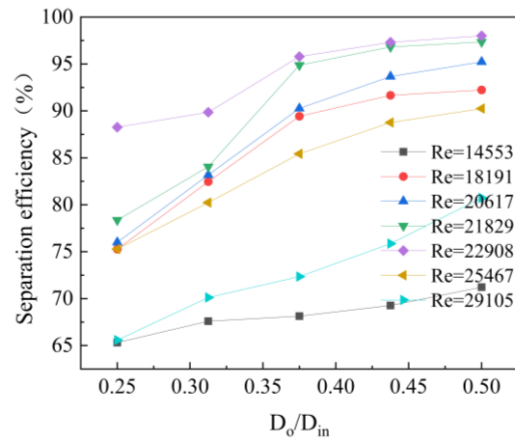

(a)

(b)

Fig. 19 Effect of Re and D_w/D_{in} on separation performance

0.563, the separation efficiency increases more gradually with the water outlet to inlet diameter ratio. Conversely, when D_w/D_{in} is greater than 0.563, the separation efficiency decreases more significantly. The influence of the ratio of the water outlet to inlet diameter on the separation efficiency remains consistent across different Reynolds numbers. However, when the Reynolds number is either larger (Re=29105) or smaller (Re=14553), the impact of the water outlet to inlet diameter ratio on separation efficiency diminishes. Figure 19(b) illustrates that the separation efficiency also exhibits an overall

trend of increasing and then decreasing with the rise in Reynolds number. The optimal separation effect for various ratios of water outlet to inlet diameter of the separator structure is achieved when the Reynolds number Re is 22908. Within the study range, the axial vortex separator performs best when Re=22908 and D_w/D_{in}=0.563, achieving the highest separation efficiency of 97.00%. The separation efficiency (η) is a parabolic function of both the Reynolds number and the ratio of the aqueous phase outlet to inlet diameter.

6.2.2 Effect of the ratio of oil outlet to inlet diameter on the separation performance

With other structural parameters held constant and the water outlet to inlet diameter ratio (D_w/D_{in}) set at 0.500, it is evident from equation (13) that the separation efficiency is a function of both the Reynolds number and the ratio of the oil outlet to inlet diameter. Figure 20 shows the relationship between different Reynolds numbers and the ratio of oil outlet to inlet diameter, and the separation performance of the axial vortex separator.

(a)
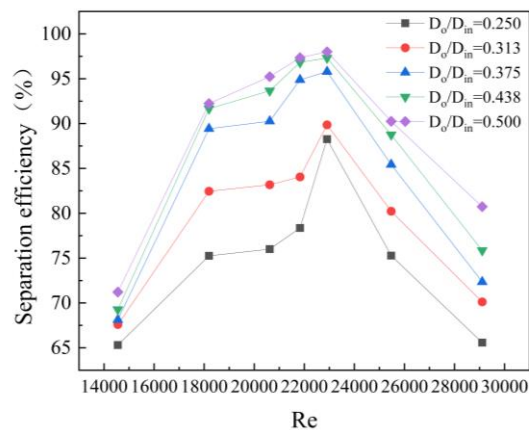
(b)

Fig. 20 Effect of Re and D_w/D_{in} on separation performance

From Fig. 20(a), it is apparent that the separation efficiency of the axial vortex separator increases with the ratio of the oil outlet to inlet diameter; that is, the

separation efficiency (η) is directly proportional to the ratio of oil outlet to inlet diameter (D_o/D_{in}). As this ratio increases, the separation efficiency gradually levels off. Given the water content at the oil outlet, a larger ratio of the oil outlet to inlet diameter is not necessarily advantageous for oil-water separation. Furthermore, the water outlet diameter is constrained by the diameter of the axial vortex separator barrel and the cone angle of the stationary barrel, which cannot be increased indefinitely. Therefore, the ratio of the oil outlet to inlet diameter (D_o/D_{in}) is always less than 1. The pattern of how the ratio of oil outlet to inlet diameter affects separation efficiency does not vary with changes in the Reynolds number. Figure 20(b) demonstrates that the influence of Reynolds number on separation efficiency for different oil outlet to inlet diameter ratios is consistent with that for different water outlet to inlet diameter ratios; i.e., the impact of the Reynolds number on separation efficiency is not altered by variations in the ratio of outlet to inlet for the two phases. In the study range, the axial vortex separator achieves its best performance when Re=22908 and D_o/D_{in}=0.500, with the highest separation efficiency being 98.01%.

6.2.3 Effect of Inlet Flow Rate and Water Content on Separation Performance

The Reynolds number in this study is primarily determined by the mixture's inlet flow rate and water content. Among the seven different Reynolds numbers discussed in the previous paper, Re=20617, Re=21829, and Re=22908 are primarily influenced by the inlet water content, corresponding to ε=0.7, ε=0.8, and ε=0.9, respectively. The variations of the remaining four Reynolds numbers, Re=14553, Re=18191, Re=21829, Re=25467, and Re=29105, are due to the changes in the mixture's inlet flow rate, corresponding to velocities of v_i=2.0 m/s, v_i=2.5 m/s, v_i=3.0 m/s, v_i=3.5 m/s, and v_i=4.0 m/s, respectively. Figure 21 illustrates the relationship between the Reynolds number and separation performance for different two-phase outlet to inlet diameter ratios.

The separation efficiency of the axial vortex separator increases with the rise in water content within the study range. When the inlet water content is 0.9, the separation efficiency of the axial vortex separator under various structural parameters is higher than under conditions with lower water content. The separation efficiency of the axial vortex separator also increases with the growth of the inlet flow rate and then decreases. Hence, it is evident that the separation efficiency of the separator is sensitive to changes in the inlet flow rate, and there exists an optimal inlet flow rate that enables the separator to achieve the best separation effect. Within the study range, the optimal separation efficiency for separators with differing structures is achieved when the inlet flow rate is 3 m/s.

7. CONCLUSION

(1) Numerical simulation was used to determine the flow field distribution law inside the axial vortex separator and to study the influence of changes in the two-phase outlet diameter on the internal flow field of
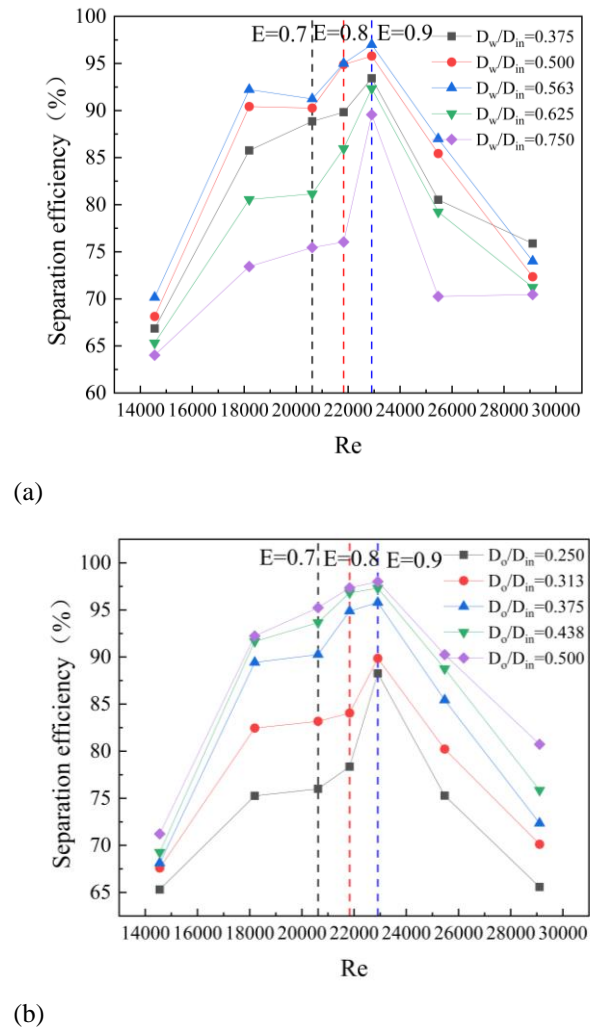
(a)

(b)

Fig. 21 Effect of Re on separation performance

the separator, which will facilitate future research and optimization of the axial vortex separator.

(2) The low-velocity reflux region formed at the water phase outlet of the axial vortex separator is fundamentally a boundary layer separation phenomenon. It results from the combined effects of the mixture's viscosity and the reverse pressure difference at the water phase outlet. This phenomenon increases the energy loss incurred as the mixture flows through the separator. In this study, the boundary layer separation phenomenon was mitigated or even eliminated by altering the aqueous phase outlet to a rounded constriction, which reduced the energy loss within the separator. When D_w equals 40 mm, the loss factor can be decreased by a maximum of 0.574.

(3) The various parameters affecting the separation performance of the axial vortex separator were analyzed utilizing the principle of dimensional analysis. It can be seen that the separation efficiency η of the separator is a function of the Reynolds number and the ratio of the two-phase outlet to the inlet diameter, with other structural parameters held constant.

(4) By examining the curves that depict the relationship between different Reynolds numbers, various ratios of two-phase outlet to inlet diameters, and the separation performance of the axial vortex separator,

it is concluded that η is directly proportional to D_o/D_{in} and is a parabolic function of Re and D_w/D_{in}. With a constant water outlet diameter, the axial vortex separator achieves the highest separation efficiency of 97.00% when D_w/D_{in} is 0.563. The separation efficiency attains its optimum at Re=22908 for different operating conditions. The efficiency increases with the rise in water content, reaching its peak when the inlet water content is 0.9, under varying structural parameters. The separation efficiency exhibits a trend of initial increase followed by a decrease as the inlet flow rate rises, reaching the optimum effect for the studied separators with different structures when v_i is 3 m/s.

CONFLICTS OF INTEREST

The authors declare no conflict of interest.

AUTHOR CONTRIBUTIONS

Conceptualization: **Huanwei Lou**; methodology: **Xingkai Zhang**, and **Huanwei Lou**; software: **Yifan Wang**; validation: **Xingkai Zhang**; formal analysis: **Huanwei Lou** and **Xuyu Liu**; investigation: **Huanwei Lou**; resources: **Huanwei Lou**; data curation: **Huanwei Lou** and **Xuyu Liu**; writing—original draft preparation: **Huanwei Lou**; writing—review and editing: **Huanwei Lou**, and **Xuyu Liu**; visualization: **Xingkai Zhang**; supervision: **Xingkai Zhang**; project administration; **Ruiguan Liao**; funding acquisition: **Xingkai Zhang**. All authors have read and agreed to the published version of the manuscript.

REFERENCES

Abrahamson, J. (2020). *Fluent Theory Guide*. http://www.ansys.com

Aghaee, M., Ganjiazad, R., Roshandel, R., & Ashjari, M. A. (2017). Two-phase flow separation in axial free vortex flow. *The Journal of Computational Multiphase Flows*, *9*(3), 105–113. https://doi.org/

H. (2023). Simulation on the influence of inlet velocity and solid separation gap on the separation characteristics of a separating device for three phases: Oil, water and solid. *Chemical Engineering Research and Design*, *189*, 179–193. https://doi.org/ 10.1016/j.cherd.2022.11.033

Gorman, J. M., Sparrow, E. M., Ilamparuthi, S., & Minkowycz, W. J. (2016). Effect of fan-generated swirl on turbulent heat transfer and fluid flow in a pipe. *International Journal of Heat and Mass Transfer*, *95*, 1019–1025. https://doi.org/ 10.1016/j.ijheatmasstransfer.2015.12.038

Guizani, R., Mhiri, H., & Bournot, P. (2022). Numerical investigation of the vortex breaker for a dynamic separator using Computational Fluid Dynamics. *Journal of Applied Fluid Mechanics*, *16*(6),1099-1107. https://doi.org/ 10.47176/jafm.16.06.1553

Ji, Y.（2015). *Theoretical & Experimental Study onto the Voraxial-Separator* (PhD. dissertation, Beijing University of Chemical Technology). https://kns.cnki.net/KCMS/detail/detail.asp

10.1177/1757482X17699411

Al-Kayiem, H. H., Hamza, J. E., & Lemmu, T. A. (2020). Performance enhancement of axial concurrent liquid–liquid hydrocyclone separator through optimization of the swirler vane angle. *Journal of Petroleum Exploration and Production Technology*, *10*(7), 2957–2967. https://doi.org/10.1007/s13202-020-00903-7

Baker, T. J. (2023). *Fluent User's Guide*. http://www.ansys.com

Boruah, M. P., Sarker, A., Randive, P. R., Pati, S., & Sahu, K. C. (2021). Tuning of regimes during two-phase flow through a cross-junction. *Physics of Fluids*, *33*(12), 122101. https://doi.org/ 10.1063/5.0071743

Celis, G. E. O., Loureiro, J. B. R., Lage, P. L. C., & Silva Freire, A. P. (2022). The effects of swirl vanes and a vortex stabilizer on the dynamic flow field in a cyclonic separator. *Chemical Engineering Science*, *248*, 117099. https://doi.org/ 10.1016/j.ces.2021.117099

Chi, Y., Zhang, R., Meng, X., Xu, J., Du, W., Liu, H., & Liu, Z. (2021). Numerical simulation of two-phase flow and droplet breakage of glycerin-water mixture and kerosene in the cyclone reactor. *Chinese Journal of Chemical Engineering*, *34*, 150–159. https://doi.org/ 10.1016/j.cjche.2021.02.021

Clausse, A., & López De Bertodano, M. (2021). Natural modes of the two-fluid model of two-phase flow. *Physics of Fluids*, *33*(3), 033324. https://doi.org/ 10.1063/5.0046189

Dyakowski, T., & Williams, R. A. (1993). Modelling turbulent flow within a small-diameter hydrocyclone. *Chemical Engineering Science*, *48*(6), 1143–1152. https://doi.org/10/ckqn3h

Gong, H., Luo, X., Peng, Y., Yu, B., Yang, Y., & Zhang,

Ji, Y., Chen, J., Cai, X., Shang, C., & Zhang, M. (2017). Design and experimental study of vortex generator based on neural network. *China Petroleum Machinery*, *45*(3), 75–84. https://doi.org/10.16082/j.cnki.issn.1001-4578.2017.03.017.

Ji, Y., Chen, J., Jiao, X., Cai, X., & Li, P. (2015). Theoretical Modeling and numerical simulation of axial-vortex separation technology used for oily water treatment. *Separation Science and Technology*, *50*(12), 1870–1881. https://doi.org/ 2023,16(6):1099-1107

Ji, Y., Chen, J., Zhou, D., Li, C., Li, R., Zhou, S., & Gong, J. (2012). Research on the operating mechanism of axial vortex separator and the optimal cone angle of barrel. *China Petroleum Machinery*, *40*(7), 106–112. https://doi.org/10.16082/j.cnki.issn.1001-4578.2012.07.002.

Karagoz, I., Avci, A., Surmen, A., & Sendogan, O. (2013). Design and performance evaluation of a new cyclone separator. *Journal of Aerosol Science*, *59*, 57–64. https://doi.org/ 10.1016/j.jaerosci.2013.01.010

Kou, J., Jiang, Z., & Cong, Y. (2021). Separation characteristics of an axial hydrocyclone separator. *Processes*, *9*(12), 2288. https://doi.org/ 10.3390/pr9122288

Liu, H., Xu, J., Wu, Y., & Zheng, Z. (2010). Numerical study on oil and water two-phase flow in a cylindrical cyclone. *Journal of Hydrodynamics*, *22*(S1), 790–795. https://doi.org/ 10.1016/S1001-6058(10)60038-8

Liu, H., Xu, J., Zhang, J., Sun, H., Zhang, J., & Wu, Y. (2012). Oil/Water separation in a liquid-liquid cylindrical cyclone. *Journal of Hydrodynamics*, *24*(1), 116–123. https://doi.org/ 10.1016/S1001-6058(11)60225-4

Versteeg, H. K., & Malalasekera, W. (2007). *An introduction to computational fluid dynamics: The finite volume method* (2nd ed). Pearson Education Ltd. https://www.pearsoned.co.uk

Young, G. A. B., Wakley, W. D., Taggart, D. L., Andrews, S. L., & Worrell, J. R. (1994). Oil-water separation using hydrocyclones: An experimental search for optimum dimensions. *Journal of Petroleum Science and Engineering*, *11*(1), 37–50. https://doi.org/ 10.1016/0920-4105(94)90061-2

Yu, A., Wang, C., Liu, H., & Khan, Md. S. (2021). Computational modeling of flow characteristics in three products hydrocyclone screen. *Processes*, *9*(8), 1295. https://doi.org/ 10.3390/pr9081295

Zandie, M., Kazemi, A., Ahmadi, M., & Moraveji, M. K. (2021). A CFD investigation into the enhancement of down-hole de-oiling hydro cyclone performance. *Journal of Petroleum Science and Engineering*, *199*, 108352. https://doi.org/10.1016/j.petrol.2021.108352

Zhang, J., He, Y. T., Liu, S., & Xu, J. Y. (2022). Oil-water separation in a cylindrical cyclone with vortex finder. *Physics of Fluids*, *34*(3), 033314. https://doi.org/ 10.1063/5.0085029

Zhu, D. Z., Han, D., He, W. F., Chen, J. J., Ji, Y. Y., Peng, T., & Gu, Y. W. (2022). Optimization and assessment of the comprehensive performance of an axial separator by response surface methodology. *Journal of Applied Fluid Mechanics*, *16*(1). https://doi.org/10.47176/jafm.16.01.1367